Journal of Applied Physics

RESEARCH ARTICLE | MARCH 05 2026

Low through-plane thermal conductivity in amorphous HfO_2/SiO_2 nanolaminates

Felix Mende; Oliver Ostien; Fred Schöne; Roman Potjan; Isabelle V. Sprave; Denny Dütz; Jan Frede; Tommy Meier; Hans Kleemann; Marcus Wislicenus; Benjamin Lilienthal-Uhlig; Lukas M. Eng

Check for updates

J. Appl. Phys. 139, 095105 (2026)
https://doi.org/10.1063/5.0312700

View Online
Export Citation

Articles You May Be Interested In

Thermal conductivity and refractive index of hafnia-alumina nanolaminates

J. Appl. Phys. (August 2011)

Dielectric performance of hybrid alumina-silicone nanolaminates synthesized by plasma enhanced chemical vapor deposition

J. Vac. Sci. Technol. A (October 2011)

Atomic layer deposited high-κ nanolaminates for silicon surface passivation

J. Vac. Sci. Technol. B (January 2014)

AIP Publishing

Journal of
Applied Physics

ARTICLE

pubs.aip.org/aip/jap

Low through-plane thermal conductivity in amorphous HfO_2/SiO_2 nanolaminates

Cite as: J. Appl. Phys. **139**, 095105 (2026); doi: 10.1063/5.0312700
Submitted: 18 November 2025 · Accepted: 13 February 2026 ·
Published Online: 5 March 2026

Felix Mende,[1,2,a)] Oliver Ostien,[1] Fred Schöne,[1] Roman Potjan,[1] Isabelle V. Sprave,[3] Denny Dütz,[3] Jan Frede,[2] Tommy Meier,[2] Hans Kleemann,[2] Marcus Wislicenus,[1] Benjamin Lilienthal-Uhlig,[1] and Lukas M. Eng[2,4]

AFFILIATIONS

[1] Fraunhofer Institute for Photonic Microsystems IPMS (Center Nanoelectronic Technologies, CNT), 01109 Dresden, Germany
[2] Institute of Applied Physics, TU Dresden, Nöthnitzer Strasse 61, 01187 Dresden, Germany
[3] JARA-FIT Institute for Quantum Information, Forschungszentrum Jülich GmbH and RWTH Aachen University, 52074 Aachen, Germany
[4] ct.qmat: Dresden-Würzburg Cluster of Excellence—EXC 2147, TU Dresden, 01062 Dresden, Germany

[a)] **Author to whom correspondence should be addressed:** felix.mende@ipms.fraunhofer.de

ABSTRACT

Accurate knowledge of thermal transport in amorphous oxides is essential for effective thermal management in advanced semiconductor and cryogenic electronic devices. In this work, we investigate the through-plane thermal conductivity (κ_z) of amorphous HfO_2/SiO_2 nanolaminates fabricated by atomic layer deposition across the temperature range from 30 to 315 K. These multilayers serve as a model system for studying heat transport in amorphous thin films, where interfacial effects may significantly influence thermal conduction. Thermal conductivities were determined using the differential 3ω method and analyzed within the framework of the heat equation. A composite model combining the minimum thermal conductivity approach for the individual amorphous layers with the diffuse mismatch model for interfacial effects quantitatively reproduces the experimental data. The multilayers exhibit low thermal conductivities of 0.77 ± 0.08 and $0.050 \pm 0.0015\,\mathrm{W\,m^{-1}\,K^{-1}}$ at 300 and 30 K, respectively.

I. INTRODUCTION

The relentless dimensional scaling of three-dimensional semiconductor architectures, such as fin field-effect transistors (FinFETs)[1–6] and gate-all-around FETs (GAAFETs),[3,7,8] has rendered thermal management a central challenge for continued CMOS technology advancement.[9–11] Scaling-induced constraints, i.e., reduced cross-sectional area and the integration of thick high-k dielectric layers, significantly increase the effective thermal resistance. This leads to elevated device self heating and, therefore, to accelerated degradation mechanisms like bias temperature instability, hot carrier injection, and electromigration.[12,13]

Conversely, high thermal resistances can be highly advantageous in other specialized device contexts. In resistive random access memory (RRAM),[14–16] for instance, localized thermal confinement enhances the efficiency of filament formation and rupture, enabling lower power switching.[17–19] Furthermore, achieving efficient thermal isolation is vital in cryogenic electronics used for, e.g., quantum computing, where temperature-sensitive quantum devices must be shielded from the heat generated by dissipative CMOS control circuitry.[20–27]

Modern (cryogenic) transistor stacks rely on amorphous dielectric films like silicon dioxide (SiO_2)[28–31] and the high-k material hafnium dioxide (HfO_2).[3,32,33] Accurate determination of their thermal transport properties, especially when interfaced, is, therefore, highly desirable. Amorphous HfO_2/SiO_2 nanolaminates serve as an attractive model system, as the multilayer architecture enables systematic tuning of thermal resistance via stack and interface engineering while preventing HfO_2 crystallization.[34–36]

Additionally, experimental studies on fully amorphous oxide multilayers remain limited,[37–39] especially when compared to the extensive literature on metal–non-metal[40–46] and crystalline

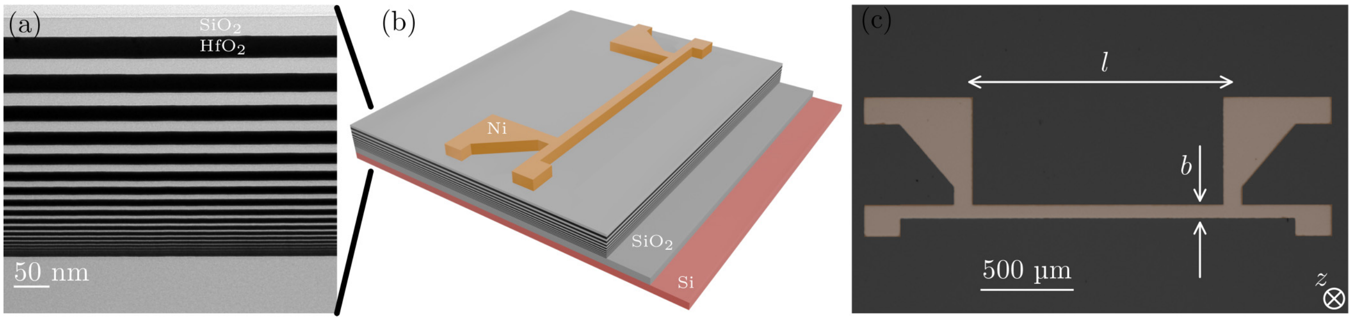

FIG. 1. (a) BF-TEM cross-sectional image of a focused ion beam lamella prepared from the graded 20-bilayer HfO_2/SiO_2 nanolaminate. (b) Schematic illustration of the nanolaminate structure: alternating HfO_2/SiO_2 layers on a nominal 100 nm SiO_2 film on a 775 μm Si (100) wafer, with a 3ω heater on top (not to scale). (c) False-colored top-down optical micrograph of a representative e-beam shadowmask-evaporated Ni 3ω heater structure used for thermal measurements. Nominally, the heater has a length of $l = 1.5$ mm, width of $b = 75 \mu$m, and thickness of $t = 60$ nm.

multilayers.[44,47–53] From a theoretical perspective, heat transport in amorphous solids is generally less well understood than in crystalline materials due to the absence of long-range order and, therefore, the breakdown of phonon-based transport models.[54–61]

Motivated by this gap in knowledge, we investigate the through-plane thermal conductivity of a technologically relevant amorphous oxide multilayer system: namely, HfO_2/SiO_2 nanolaminates. While isolated films have been studied previously,[62–65] this work provides a comprehensive characterization of their nanolaminates over a wide temperature range of 30–315 K, utilizing structures fabricated via ALD on a 300 mm wafer platform using fully CMOS-compatible processes. The resulting experimental data are analyzed within the framework of diffusive heat transport using a composite model that combines the minimum thermal conductivity approach[56,66,67] for the individual amorphous layers with the DMM[68] for interfacial effects. We observe satisfactory agreement between the measured data and the composite model, underscoring the role of interfacial effects in suppressing heat transport.

II. NANOLAMINATE DEPOSITION AND CHARACTERIZATION

A. Nanolaminate deposition

Amorphous HfO_2/SiO_2 nanolaminates were deposited using ALD on 300 mm wafer tools in a standard ISO class 6 cleanroom environment. Specifically, the amorphous HfO_2 layers were deposited in a Pulsar 3000 reactor, using hafnium chloride ($HfCl_4$) and water (H_2O) as precursors, with nitrogen (N_2) as the purge gas. The deposition was carried out at 523 K. Amorphous SiO_2 was deposited using plasma-enhanced ALD in an EmerALD process module. The process utilized BDEAS—bis(diethylamino)silane (SAM24) and oxygen as the oxidant. The plasma power was set to 50 W, and the substrate temperature was maintained at 323 K.

Using this approach, four distinct nanolaminate structures were fabricated. All multilayer samples were designed with a 1:1 total thickness ratio of amorphous HfO_2 to amorphous SiO_2. Three of the samples were non-graded, consisting of 10, 15, and 20 bilayers, respectively, each produced with a nominal single layer thickness of 10 nm.

The fourth sample was a graded 20-bilayer structure, designed to have the same total HfO_2 and SiO_2 thickness, and the same number of interfaces, as the non-graded 20-bilayer sample. The single layer thicknesses in this graded sample were varied according to an exponential growth profile, specifically designed with nominal layer thicknesses of 1.0, 1.3, 1.5, 1.8, 2.2, 2.6, 3.2, 3.8, 4.6, 5.5, 6.6, 8.0, 9.5, 11.4, 13.7, 16.5, 19.9, 23.9, 28.7, and 34.5 nm [for a visual representation, see Fig. 1(a)].

B. Bright-field transmission electron microscopy (BF-TEM)

A BF-TEM cross-sectional image of the graded HfO_2/SiO_2 multilayer is shown in Fig. 1(a). The image was acquired at an accelerating voltage of 200 kV using a Tecnai F20 microscope from Thermo Fisher Scientific. Sharp, well-defined interfaces between the individual layers are clearly observed.

C. X-ray reflectometry (XRR) measurements

The film thickness of the HfO_2/SiO_2 nanolaminates (see Table I) were estimated from XRR measurements. The measurements were performed on a Bede Metrix F diffractometer using Cu K_{α_1} radiation ($\lambda = 1.540\,56$Å) in coupled Ω–2θ geometry. An example XRR measurement is shown in Fig. 2.

D. Sputter x-ray photo electron spectroscopy (sputter-XPS)

The stoichiometry of the deposited HfO_2 and SiO_2 thin films was determined by sputter-XPS measurements. These were performed using a PHI Quantes scanning XPS/HAXPES microprobe (Physical Electronics) equipped with a monochromatic Al K_α x-ray source ($\lambda = 8.3401$Å) and an Ar^+ ion sputter source for depth profiling. Figure 3 shows a representative data set from the graded 20-bilayer HfO_2/SiO_2 sample. Atomic concentrations were calculated using corrected relative sensitivity factors, where the standard values[70] were adjusted for the instrument-specific asymmetry and transmission functions. The films exhibit stoichiometries close to their nominal values within typical XPS uncertainties, indicating

TABLE I. Summary of fabricated thin films. The table lists the nominal stack geometry, estimated total nanolaminate thickness (t_{nl}, derived from XRR measurements), and corresponding measured through-plane thermal conductivity and diffusivity (D_z) at 300 K. D_z was calculated assuming a Debye-like heat capacity (see Appendix D 1).

Nominal sample structure	t_{nl} (nm)	κ_z at 300 KW m^{-1} K^{-1}	D_z at 300 K (mm^2 s^{-1})
10-bilayer (10 nm HfO_2/10 nm SiO_2)	190 ± 4	0.86 ± 0.04	0.37 ± 0.04
15-bilayer (10 nm HfO_2/10 nm SiO_2)	274 ± 5	0.72 ± 0.02	0.31 ± 0.03
20-bilayer (10 nm HfO_2/10 nm SiO_2)	376 ± 8	0.79 ± 0.02	0.34 ± 0.04
Graded 20-bilayer HfO_2/SiO_2	375 ± 20	0.69 ± 0.02	0.30 ± 0.03

high chemical uniformity across the individual layers. The reduced modulation amplitude observed in the deeper part of the stack can be attributed to the finite information depth of XPS (several nanometers), which leads to signal averaging across multiple ultrathin layers. Additional attenuation of the layer contrast may arise from sputter-induced intermixing during the depth profiling process.

E. Thin-film x-ray diffractometry (XRD)

Complementary to the chemical analysis, XRD measurements were conducted to evaluate the structural properties of the films. The measurements were carried out using a Bruker D8 Discover diffractometer in standard θ–2θ geometry with Cu K_{α_1} radiation ($\lambda = 1.540\,56$Å). Example measurements, along with simulated diffraction patterns of potential crystalline phases, are presented in Fig. 4. The XRD results indicate that the samples are (predominantly) amorphous, as evidenced by the absence of distinct diffraction peaks.

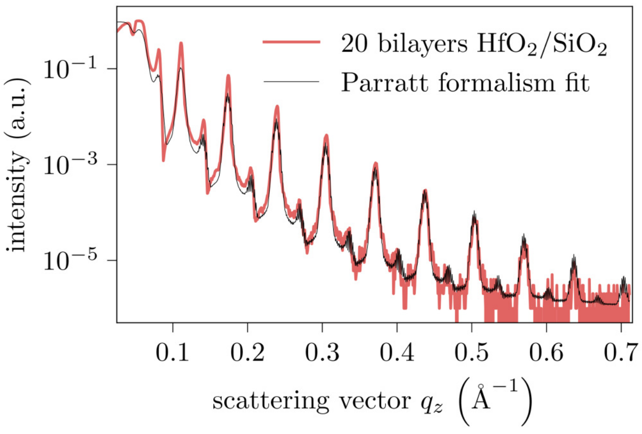

FIG. 2. XRR measurement of the non-graded 20-bilayer HfO_2/SiO_2 nanolaminate deposited on a nominal 100 nm SiO_2 layer (red), along with a Parratt-model fit (black) performed using GenX.[69] The scattering vector is defined as $q_z = \frac{4\pi}{\lambda}\sin\theta$, with the z-direction corresponding to the multilayer growth direction [see Fig. 1(c)].

F. Atomic force microscopy (AFM) measurements

To assess the surface roughness profile and identify potential microcrystalline features, AFM measurements were performed using a Cypher S system (Asylum Research). Scans were acquired on a $1 \times 1\mu m^2$ area with a 512×512 equidistant point grid. Measurements employed Bruker OLTESPA-R3 probes, characterized by a nominal tip radius of 7 nm. Tip integrity was routinely verified using a TipCheck calibration standard (BudgetSensors) to maintain measurement accuracy.[72] Representative surface roughness plots for the N-bilayer HfO_2/SiO_2 samples and the graded 20-bilayer HfO_2/SiO_2 samples are shown in Figs. 5(a) and 5(b), respectively. The N-bilayer samples, with a nominal layer thickness of 10 nm, exhibit a typical random rough surface characteristic of amorphous thin films. In contrast, Fig. 5(b) reveals features suggestive of sparsely distributed nanocrystallites on the order of a few tens of nanometers. These are most likely attributed to the thicker HfO_2 layers near the surface of the graded 20-bilayer HfO_2/SiO_2 sample.[34–36] The potential nanocrystalline features of the graded 20-bilayer HfO_2/SiO_2 sample might not have been detected by XRD measurements due to their low volume fraction and small size, which reduce the diffraction signal below the detection threshold.

III. THERMAL CONDUCTIVITY MEASUREMENTS AND RESULTS

We determined κ_z of our HfO_2/SiO_2 nanolaminates using the differential 3ω method.[63,73,74] For this purpose, 60 nm-thick Ni thin-film heaters/thermometers were fabricated directly on top of the nanolaminates by electron-beam evaporation through a shadow mask [see Figs. 1(b) and 1(c)].

A. Differential 3ω method: Determination of κ_z

The nanolaminates under investigation consist of very thin alternating amorphous HfO_2 and SiO_2 layers deposited on a nominal 100 nm thick amorphous SiO_2 layer, supported by a thick 775 μm silicon substrate [see Figs. 1(a) and 1(b)]. The through-plane thermal conductivity was determined by probing the temperature response of the nanolaminate to an alternating (AC) heating current. The thermal response is modeled within the framework of the heat equation, where each material is assigned an intrinsic κ_z value. Additionally, the influence of the material interfaces is incorporated by introducing a finite-valued interface thermal conductance (G_{HfO_2,SiO_2}).

In the thin-film limit, where the total nanolaminate thickness t_{nl} is much smaller than the heater width b [see Figs. 1(a) and 1(c)], lateral heat spreading within the nanolaminate is physically negligible, which renders the measurement primarily sensitive to the through-plane thermal conductivity κ_z while losing sensitivity toward the in-plane direction.[49,74] Consequently, when the system is subjected to spatially isotropic heating at an angular frequency ω_h from the top of the stack, the resulting peak temperature amplitude at the nanolaminate surface is expressible as

$$T_{Si/SiO_2/[HfO_2/SiO_2]_N}(\omega_h) = T_{Si/SiO_2}(\omega_h) + J\left(\frac{2N}{G_{HfO_2,SiO_2}} + \frac{\sum_i t_{HfO_2,i}}{\kappa_{z,HfO_2}} + \frac{\sum_j t_{SiO_2,j}}{\kappa_{z,SiO_2}}\right). \quad (1)$$

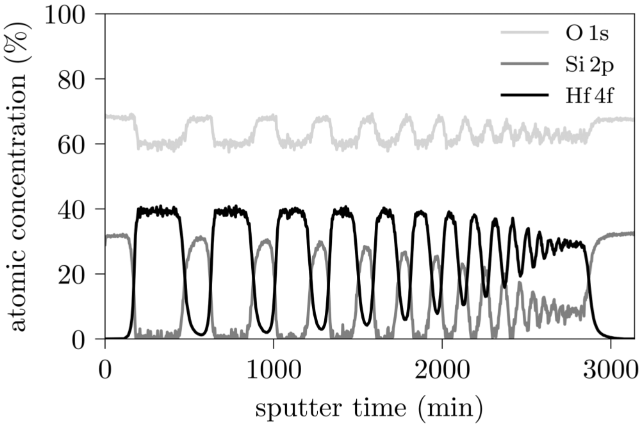

FIG. 3. Sputter-XPS measurements of the graded 20-bilayer HfO_2/SiO_2 nanolaminate on the 100 nm SiO_2 sample.

Here, $T_{Si/SiO_2}(\omega_h)$ is the hypothetical peak temperature amplitude of the bare substrate in the absence of the nanolaminate,

$$J = \frac{P}{bl} \tag{2}$$

is the peak amplitude of the applied sinusoidal heat current (P) per unit area (bl) and G_{HfO_2,SiO_2} is the thermal boundary conductance of the HfO_2/SiO_2 interface. The indices i and j label the individual HfO_2 and SiO_2 layers, respectively, across the N bilayer stack.

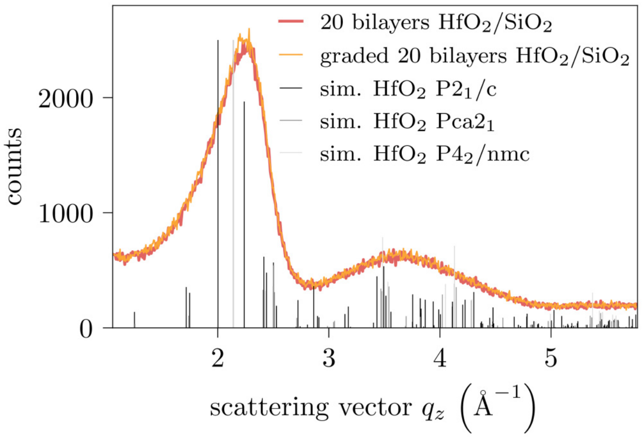

FIG. 4. XRD measurements of non-graded (red) and graded (orange) 20-bilayer HfO_2/SiO_2 nanolaminate on 100 nm amorphous *SiO_2* samples. The absence of distinct diffraction peaks indicates that the samples are (predominantly) amorphous. Simulated diffraction patterns were generated using data from the Materials Project database (database version v2025.09.25), licensed under a Creative Commons Attribution (CC BY) license.[71]

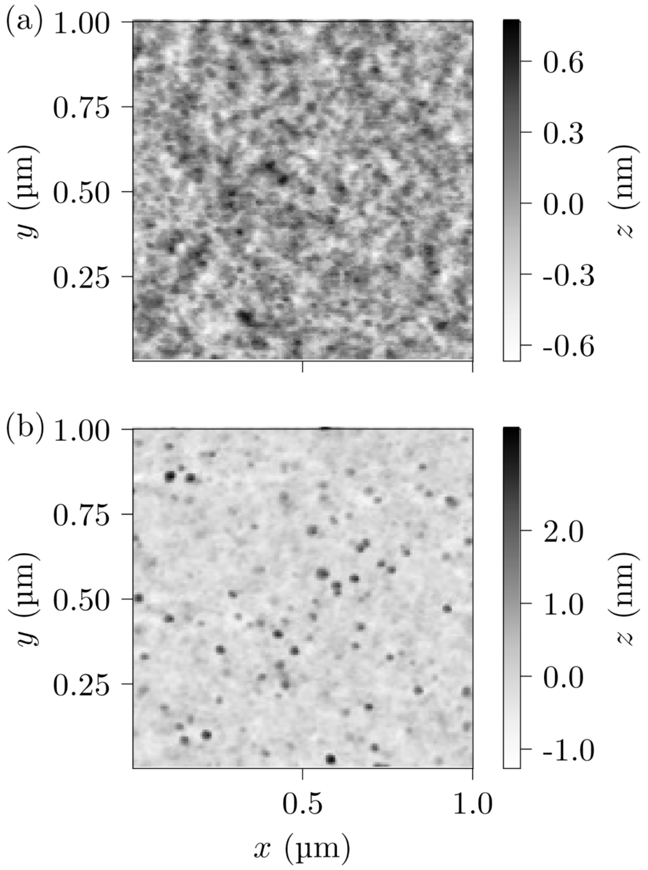

FIG. 5. AFM measurements of the 20-bilayer HfO_2/SiO_2 nanolaminate samples. (a) The non-graded structure and (b) the graded structure.

Equation (1) illustrates that intrinsic and interfacial contributions to the thermal resistance enter additively and are not directly separable in this configuration. We, therefore, introduce an effective medium description characterized by an effective through-plane thermal conductivity ($\kappa_{z,\mathrm{eff}}$).

As a starting point, we consider the total nanolaminate thickness,

$$t_{\mathrm{nl}} = \sum_i t_{HfO_2,i} + \sum_j t_{SiO_2,j}. \tag{3}$$

Then, the average intrinsic conductivity $\kappa_{z,\mathrm{avg}}$ is defined by the weighted harmonic mean,

$$\frac{1}{\kappa_{z,\mathrm{avg}}} := \frac{\sum_i t_{HfO_2,i}}{t_{\mathrm{nl}}} \frac{1}{\kappa_{z,HfO_2}} + \frac{\sum_j t_{SiO_2,j}}{t_{\mathrm{nl}}} \frac{1}{\kappa_{z,SiO_2}}. \tag{4}$$

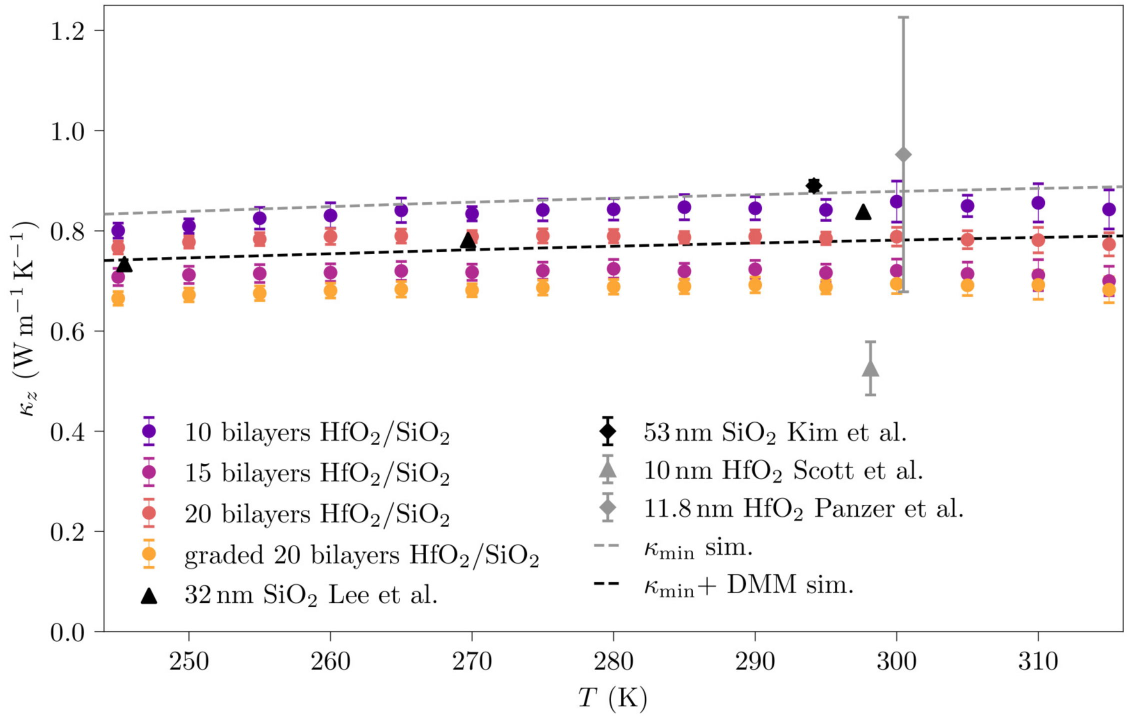

FIG. 6. Temperature-dependent thermal conductivity of amorphous HfO_2/SiO_2 nanolaminates (colored solid circles). The data are shown from 245 to 315 K and are compared with literature values extracted for SiO_2 thin films (Lee and Cahill[62] and Kim *et al.*[63]) (black symbols) and HfO_2 thin films (Scott *et al.*[65] and Panzer *et al.*[64]) (gray symbols). Also shown are model predictions: the estimated minimum thermal conductivity of the nanolaminate [gray dashed, see Eq. (D8)] and a composite model additionally incorporating thermal boundary resistance via the DMM [black dashed, see Eq. (D9)].

Substituting this into Eq. (1) yields

$$T_{\mathrm{Si/SiO_2/[HfO_2/SiO_2]}_N}(\omega_h) = T_{\mathrm{Si/SiO_2}}(\omega_h) + J\underbrace{\left(\frac{2N}{G_{\mathrm{HfO_2,SiO_2}}t_{\mathrm{nl}}} + \frac{1}{\kappa_{z,\mathrm{avg.}}}\right)}_{=:\frac{1}{\kappa_{z,\mathrm{eff}}}} t_{\mathrm{nl}}. \tag{5}$$

Notice that $\kappa_{z,\mathrm{eff}}$ is a function of the interface density $(\frac{2N}{t_{\mathrm{nl}}})$ and the relative amounts of HfO_2 and SiO_2 in the nanolaminate.

Experimentally, $\kappa_{z,\mathrm{eff}}$ is determined by measuring two samples under identical conditions: one containing the nanolaminate and a reference sample without it. The resulting expression is

$$\kappa_{z,\mathrm{eff}} = \left(\frac{T_{\mathrm{Si/SiO_2/[HfO_2/SiO_2]}_N}}{J_{\mathrm{Si/SiO_2/[HfO_2/SiO_2]}_N}} - \frac{T_{\mathrm{Si/SiO_2}}}{J_{\mathrm{Si/SiO_2}}}\right)^{-1} t_{\mathrm{nl}}. \tag{6}$$

Ideally, the applied heat fluxes for the nanolaminate and reference sample measurements are nearly identical ($J_{\mathrm{Si/SiO_2/[HfO_2/SiO_2]}_N} \approx J_{\mathrm{Si/SiO_2}}$). However, small deviations may arise due to fabrication tolerances and measurement uncertainties.

B. Near-room-temperature thermal conductivity measurements and results

1. Measurement details

Near-room-temperature thermal conductivity measurements were conducted over a temperature range of 245–315 K. The prepared samples featuring the 3ω metal structures [see Fig. 1(c)] were adhered to a copper sample holder using GE 7031 Varnish. Electrical connections were made via 25 μm AlSiCu wire bonds to a custom-designed printed circuit board (PCB). The complete PCB-mounted assembly was placed on the temperature-controlled chuck of a FormFactor CM300xi probe station, where a continuous laminar flow of dry air was maintained to prevent condensation during measurement.

2. Results and discussion

Results for the measured thermal conductivities are presented in Fig. 6. For context and comparison, the figure also includes established literature values for thin films of the constituent materials: SiO_2 data from Lee and Cahill[62] and Kim *et al.*,[63] and HfO_2 data from Panzer *et al.*[64] and Scott *et al.*[65] In addition to the experimental data, two theoretical predictions are shown: the minimum thermal conductivity based on the intrinsic layer properties (Appendix D 3), and a composite model that also incorporates the finite thermal boundary conductance of the HfO_2/SiO_2 interfaces using the DMM (Appendix D 4).

At 300 K, the composite model predicts an effective through-plane conductivity of $\kappa_{\mathrm{min+DMM}} = 0.78\,\mathrm{W\,m^{-1}\,K^{-1}}$, derived from an intrinsic minimum conductivity of $\kappa_{\mathrm{min}} = 0.88\,\mathrm{W\,m^{-1}\,K^{-1}}$ together with a DMM-calculated interface conductance of $G_{\mathrm{HfO_2,SiO_2}} = 750\,\mathrm{MW\,m^{-2}\,K^{-1}}$ [see Eq. (5)].

Given the multilayer geometry (Sec. II A, Table I) and assuming purely diffusive heat transport [Eq. (5)], all samples are expected to show the same effective thermal conductivity value. Indeed, we measure a consistent average of $\mathbf{0.77 \pm 0.08}\,\mathrm{W\,m^{-1}\,K^{-1}}$ at 300 K, in good agreement with the composite model. The observed spread is consistent with the $\approx 10\%$ uncertainty determined from our simultaneous Si substrate calibration (Appendix B) and comparable to typical experimental uncertainties reported in the literature.[75]

Moreover, although all samples are expected to exhibit identical effective thermal conductivities under the assumption of purely diffusive transport, the graded nanolaminate exhibits a slightly lower average conductivity than the uniform non-graded structures. This difference lies within the experimental uncertainty and is, therefore, not statistically significant. Nevertheless, the sign of this deviation is consistent with prior theoretical and simulation studies on crystalline, graded, and non-periodic superlattices, which report an enhanced suppression of long-wavelength and long-mean-free-path vibrational modes due to increased structural aperiodicity, mode localization, and disruption of coherent transport pathways.[76–80] In addition, one cannot fully exclude contributions from local structural variations, such as potential microcrystalline features in the thicker HfO_2 layers indicated by the AFM analysis, which could introduce additional vibrational mode scattering or localization.[81]

C. Low-temperature thermal conductivity measurements

1. Measurement details

Low-temperature differential 3ω thermal conductivity measurements were performed using a Kiutra L-Type Rapid cryostat. To ensure optimal thermal contact, the samples were adhered with silver paste to a gold-plated, oxygen-free copper sample holder, which is a component of the Kiutra 32 DC puck sample carrier pad. The four-point measurement structures were then wire-bonded using 25 μm AlSiCu wires to the PCB of the sample carrier.

2. Results and discussion

The measured low-temperature thermal conductivities are presented in Fig. 7. For comparison, the figure includes reference values for bulk amorphous SiO_2 from Touloukian *et al.*,[82] as well as our own measurements of a 500 nm amorphous SiO_2 thin film.

As in the near-room-temperature analysis, two model predictions are shown: the minimum thermal conductivity based on intrinsic layer properties (Appendix D 3) and a composite model incorporating interface resistance using the DMM (Appendix D 4). At 30 K, the

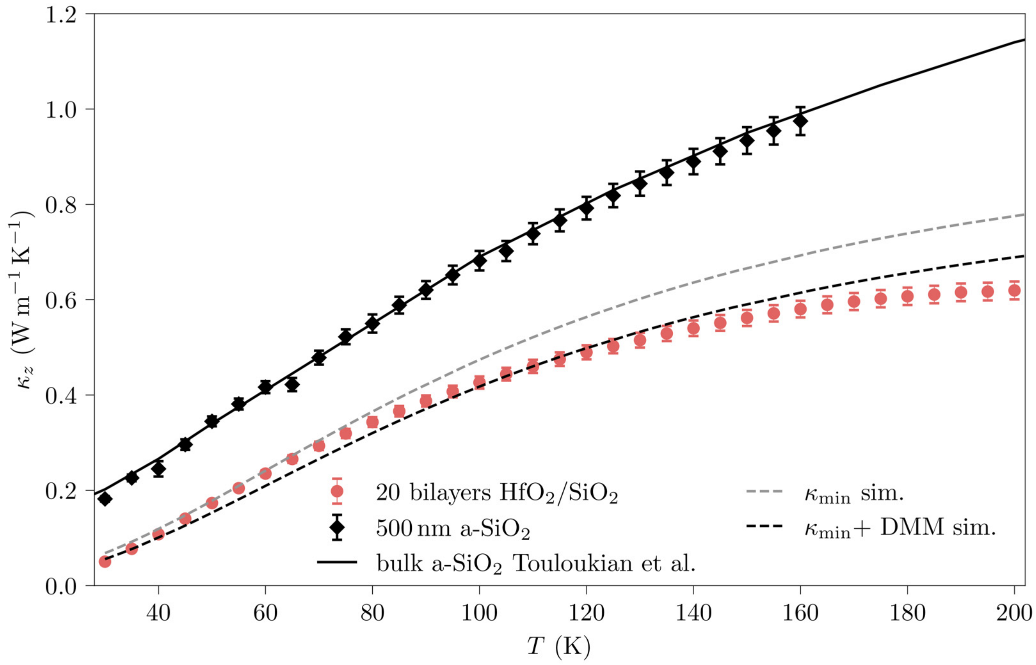

FIG. 7. Measured temperature-dependent through-plane thermal conductivity of the amorphous 20-bilayer (10 nm HfO_2/10 nm SiO_2) nanolaminate (red solid circle). For comparison, the data include our own measurements of a 500 nm amorphous SiO_2 thin film (black diamond), as well as literature reference values for bulk amorphous SiO_2 digitally plotted from the tabulated data of Touloukian *et al.*[82] (black line). Also shown are model predictions: the estimated minimum thermal conductivity of the nanolaminate [gray dashed, see Eq. (D8)] and a composite model incorporating thermal boundary resistance via the DMM [black dashed, see Eq. (D9)].

composite model predicts an effective thermal conductivity of $\kappa_{\min+\mathrm{DMM}} = 0.056\,\mathrm{W\,m^{-1}\,K^{-1}}$, derived from an intrinsic minimum conductivity of $\kappa_{\min} = 0.068\,\mathrm{W\,m^{-1}\,K^{-1}}$ and a DMM-calculated interface conductance of $G_{\mathrm{HfO_2,SiO_2}} = 32\,\mathrm{MW\,m^{-2}\,K^{-1}}$ [see Eq. (5)].

Experimentally, we find that the multilayer exhibits a substantially lower thermal conductivity than the amorphous 500 nm SiO_2 film across the entire low-temperature range. At 30 K, the 20-bilayer HfO_2/SiO_2 sample reaches $\kappa_z = 0.050 \pm 0.0015\,\mathrm{W\,m^{-1}\,K^{-1}}$, corresponding to only 28% of the SiO_2 thin-film value at the same temperature.

A simple contributing factor to the reduced thermal conductivity of the HfO_2/SiO_2 nanolaminates may be the lower mass density of the ALD-grown films compared to their bulk counterparts (see Table II).

A comparison of Figs. 6 and 7 reveals an offset between the two measurement series. We attribute this discrepancy primarily to inherent measurement uncertainties, arising from factors such as heater-to-heater fabrication variations, limited precision in determining the heater width, and uncertainties in the highly sensitive temperature-coefficient-of-resistance measurement.

Overall, the low-temperature behavior of the nanolaminate is well reproduced by the composite minimum thermal conductivity + DMM model. However, this agreement must be viewed with care: the model's predicted $\kappa_{\min}$ for SiO_2 at 30 K ($0.058\,\mathrm{W\,m^{-1}\,K^{-1}}$) is significantly lower than both our measured value for the 500 nm amorphous SiO_2 film and established bulk data. This discrepancy is well known from the literature, particularly at low temperatures, where low-frequency, long-wavelength vibrational modes enhance thermal transport beyond the purely diffusive minimum conductivity picture.[56,57,66,67,83,84]

From this perspective, the success of the composite model in fitting the multilayer data suggests an interesting possibility. Due to the high density of thin, highly uniform layers, the nanolaminate configuration may effectively suppress these long-wavelength contributions that are otherwise present in bulk amorphous SiO_2. Put cautiously, our results are consistent with the interpretation that the multilayer geometry acts as a filter for certain long-wavelength vibrational modes, suppressing wave-like thermal transport and thereby driving the system closer to the minimum conductivity limit even at low temperatures.

IV. SUMMARY AND OUTLOOK

We experimentally investigated thermal transport in amorphous HfO_2/SiO_2 nanolaminates fabricated by ALD on a 300 mm wafer platform under CMOS-compatible conditions. These nanolaminates provide a well-controlled model system for studying heat conduction across amorphous oxide interfaces relevant to modern semiconductor and cryogenic electronic devices.

Using the differential 3ω method, we determined κ_z over the temperature range of 30–315 K, finding low values of $(0.77 \pm 0.08)\,\mathrm{W\,m^{-1}\,K^{-1}}$ at 300 K and $(0.0500 \pm 0.0015)\,\mathrm{W\,m^{-1}\,K^{-1}}$ at 30 K. These values lie substantially below the corresponding conductivity of amorphous SiO_2, with the strongest suppression at 30 K, where the nanolaminate reaches only 28% of the amorphous SiO_2 value.

The measured data are well reproduced by a composite model, combining the minimum thermal conductivity model[56,66,67] with the DMM[68] for interfaces. This agreement is particularly notable at low temperatures, given that the $\kappa_{\min}$ model is known to underestimate the measured thermal conductivity of bulk amorphous materials, a discrepancy often attributed to enhanced wave-like thermal transport.[56,57,66,67,83,84] The good agreement suggests that the multilayer structure is highly effective in suppressing these wave-like, long-wavelength vibrational modes, thereby extending the validity of the purely diffusive $\kappa_{\min}$ limit. While our model provides a robust empirical description, a more fundamental atomistic understanding of heat transport in complex amorphous nanostructures remains an open challenge (see Appendix D 5).

Future work should, therefore, pursue both experimental and theoretical progress. Experimentally, systematic variation of the layer thickness and interface density may help to isolate interfacial and intrinsic contributions, if separable, to the overall thermal resistance. Moreover, investigating stochastic stacking, such as fully randomized layer thickness arrangements, may represent an additional promising route to further reduce through-plane thermal conductivity.[76–80] Furthermore, extending measurements to temperatures well below 30 K could make any wave-like related effects more pronounced, potentially opening pathways to engineer phononic bandgaps or, more generally, to tailor thermal transport.[51,52,78,85,86] On the theoretical side, scaling atomistic transport simulations to experimentally relevant dimensions remains an important challenge. Together, such developments could enable the realization of oxide-based multilayers with tunable and potentially engineered thermal conductivities, being of direct relevance to next-generation logic, cryogenic, and quantum electronic applications.

ACKNOWLEDGMENTS

This work was funded by the German Federal Ministry of Research, Technology and Space (BMFTR) within the framework programme "Quantum technologies—from basic research to market" (Project QSolid, Grant No. 13N16150).

AUTHOR DECLARATIONS

Conflict of Interest

The authors have no conflicts to disclose.

Author Contributions

Felix Mende: Conceptualization (lead); Data curation (lead); Formal analysis (lead); Investigation (lead); Methodology (lead); Project administration (lead); Software (lead); Validation (lead); Visualization (lead); Writing – original draft (lead); Writing – review & editing (lead). **Oliver Ostien:** Data curation (supporting); Methodology (supporting); Validation (supporting); Visualization (supporting); Writing – original draft (supporting); Writing – review & editing (equal). **Fred Schöne:** Data curation (supporting); Methodology (supporting); Writing – original draft (supporting); Writing – review & editing (equal). **Roman Potjan:** Data curation (supporting); Methodology (supporting); Writing – original draft (supporting); Writing – review & editing (equal). **Isabelle V. Sprave:**

Data curation (supporting); Methodology (supporting); Writing – original draft (supporting); Writing – review & editing (equal). **Denny Dütz:** Data curation (supporting); Methodology (supporting); Writing – original draft (supporting); Writing – review & editing (equal). **Jan Frede:** Data curation (supporting); Methodology (supporting); Writing – original draft (supporting); Writing – review & editing (equal). **Tommy Meier:** Data curation (supporting); Methodology (supporting); Writing – original draft (supporting); Writing – review & editing (equal). **Hans Kleemann:** Data curation (supporting); Methodology (supporting); Writing – original draft (supporting); Writing – review & editing (equal). **Marcus Wislicenus:** Data curation (supporting); Funding acquisition (lead); Project administration (equal); Writing – original draft (supporting); Writing – review & editing (equal). **Benjamin Lilienthal-Uhlig:** Data curation (supporting); Funding acquisition (lead); Methodology (supporting); Writing – original draft (supporting); Writing – review & editing (equal). **Lukas M. Eng:** Conceptualization (supporting); Data curation (supporting); Methodology (supporting); Writing – original draft (supporting); Writing – review & editing (equal).

DATA AVAILABILITY

The data that support the findings of this study are available from the corresponding author upon reasonable request.

APPENDIX A: 3ω MEASUREMENT DETAILS

To drive a sinusoidal electrical current at an angular frequency ω through the line heater, a Keithley 6221 precision AC current source was employed. The resulting 1ω and 3ω voltage amplitudes were extracted using a phase synchronized Zurich Instruments MFLI lock-in amplifier. To determine the temperature-dependent resistance of the line heaters, 1ω characterization was performed with a peak current amplitude of 5 mA at a frequency of 401 Hz. This allowed for the precise determination of the resistance R_0 and the temperature coefficient of resistance (TCR), α, at each respective substrate temperature setpoint. For the 3ω measurements, the peak current amplitude was adjusted based on the temperature regime to maintain an optimal signal-to-noise ratio. A peak current of 45 mA was utilized for measurements near room temperature, while 30 mA was used for the low-temperature characterization. Although current frequencies between 10 and 6000 Hz were recorded, the evaluations were restricted to the range between 100 and 2000 Hz. This specific window was chosen to limit the thermal penetration depth according to the criteria described by Dames[74] and to ensure that the measurements remained within the validity regime of the low-frequency approximations of the heat equation.

The measured 3ω peak voltage amplitudes were converted into temperature peak amplitudes following Ref. 74,

$$T_{2\omega} = \frac{2U_{3\omega}}{I_{1\omega}R_0\alpha}. \tag{A1}$$

Here, $T_{2\omega}$ denotes the peak amplitude of the oscillating line-heater temperature, $T(t) = T_{2\omega}\cos(2\omega t + \phi)$, induced by Joule heating. $I_{1\omega}$ is the applied peak current amplitude. R_0 is the heater resistance determined from the 1ω measurements, and $\alpha := \frac{1}{R}\frac{dR}{dT}$ is the corresponding TCR at the respective substrate temperature.

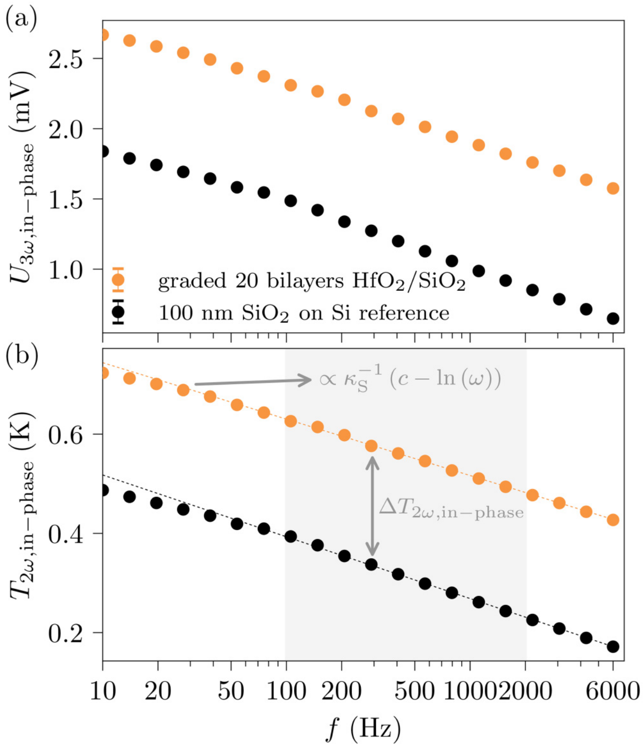

FIG. 8. Representative 3ω measurement data at 300 K. Data are shown for the graded HfO$_2$/SiO$_2$ nanolaminate on 100 nm SiO$_2$/Si and a reference sample consisting of 100 nm SiO$_2$ on Si. (a) Measured 3ω in-phase peak voltage amplitude, $U_{3\omega,\text{in-phase}}$, as a function of the current frequency. (b) Extracted in-phase peak temperature oscillations, $T_{2\omega,\text{in-phase}}$, derived from the 3$\omega$ voltage using Eq. (A1). The shaded region indicates the frequency window used for the point-by-point thermal conductivity evaluation. Dashed lines represent corresponding linear fits within this region and are extrapolated as a guide for the eye.

Typical temperature amplitudes were in the range of 0.1–1 K for all measured samples and references in the temperature region above 50 K. At lower temperatures, the temperature amplitudes increase markedly, reaching values up to approximately 2.7 K at a substrate temperature of 30 K. Due to this rising temperature amplitudes and the rapidly decreasing temperature sensitivity of the nickel thin films, characterization was limited to the region above 30 K to maintain measurement accuracy. The upper limit of 315 K was dictated by stability considerations of our specific experimental setup rather than a fundamental limitation of the 3ω approach itself. Example measurement data for the measured 3ω peak voltage amplitudes and corresponding peak temperature amplitudes are shown in Figs. 8(a) and 8(b), respectively. The nanolaminates' thermal conductivities were evaluated point by point according to Eq. (6) using the extracted in-phase temperature amplitude signal ($T_{2\omega,\text{in-phase}}$).[74] Uncertainties are given as the sample standard deviation of the set of point evaluations.

A major challenge in performing 3ω measurements is that the voltage signal of interest, $U_{3\omega}$, is typically orders of magnitude smaller than the linear ohmic response, $U_{1\omega}$. To address this, we followed the common literature approach of subtracting a large fraction of the $U_{1\omega}$ signal.[74] Suppressing the dominant 1ω component is essential for effectively utilizing the lock-in amplifier's dynamic reserve by enabling higher gain preamplification, thereby ensuring an optimal signal-to-noise ratio.[74,87] In our implementation, $U_{1\omega}$ voltage subtraction is achieved by placing a potentiometer (Vishay precision 534, 200Ω) with intrinsically low $U_{3\omega}$ signal generation in series with 3ω device under test. The dominant $U_{1\omega}$ signal is then suppressed using an analog subtraction circuit,[87] as illustrated schematically in Fig. 9. To ensure precise and repeatable balancing, the potentiometer is automatically adjusted using a PC-controlled stepper motor assembly.

The heater dimensions ($b = 75\,\mu$m, $l = 1.5$ mm) were selected to balance the physical requirements of the 1D thin-film limit with the practical constraints of our experimental hardware. A width of $75\,\mu$m was chosen to ensure reliable, lithography-free fabrication via shadow masking while minimizing relative geometric uncertainties. Furthermore, the resulting high heater-width-to-film-thickness ratio ($b/d_\mathrm{f} > 187$) physically restricts heat spreading to the through-plane direction and provides effective spatial averaging over the sample surface.[49,74] From an electrical perspective, the length l was designed to maintain a heater resistance below 80Ω across all measured temperatures. This ensures that the peak electrical currents required to generate temperature oscillations of 0.1–1 K (up to 50 mA) do not exceed the 5 V linear operating limit of the analog subtraction circuit sketched in Fig. 9.

Lastly, we briefly address the potential influence of the steady, laminar dry air flow and radiative losses on the room-temperature thermal conductivity estimates. The dissipated Joule heating power has an amplitude on the order of 60 mW. To assess the impact of environmental losses, we conservatively estimate a convective heat transfer coefficient of $h_\mathrm{conv} \approx 100\,\mathrm{W\,m^{-2}\,K^{-1}}$ and a radiative coefficient of $h_\mathrm{rad} < 10\,\mathrm{W\,m^{-2}\,K^{-1}}$ across the measured temperature ranges.[88] Even assuming an atypically high combined heat transfer coefficient of $h_\mathrm{rad+conv} = 1000\,\mathrm{W\,m^{-2}\,K^{-1}}$, the ratio of environmental losses to conductive power remains negligible,

$$\frac{P_\mathrm{rad+conv}}{P_{2\omega}} < 0.3\%. \tag{A2}$$

Dames arrived at the same conclusion using a slightly different argument in Sec. 2.3.3 of Ref. 74.

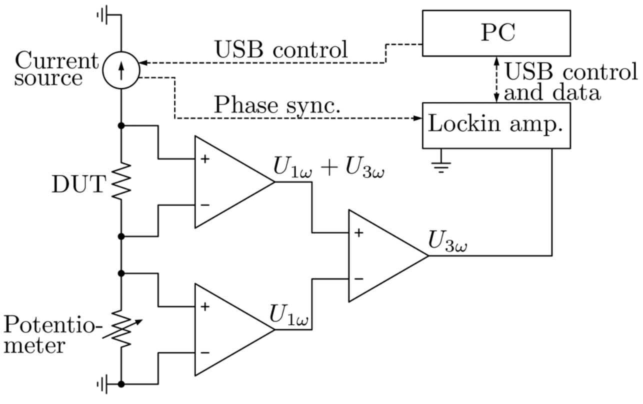

FIG. 9. Schematic of the 3ω measurement setup. A sinusoidal electrical current at frequency 1ω is applied to the device under test (DUT) and a reference potentiometer. The resulting voltage drops are subtracted using an analog subtraction circuit and the differential signal is fed into a lock-in amplifier for detection of the 3ω component. Adapted with permission from Erfantalab *et al.*, Int. J. Heat Mass Transfer **184**, 122346 (2022). Copyright 2022 Elsevier.[87]

APPENDIX B: 3ω MEASUREMENT SETUP VALIDATION: Si SUBSTRATE THERMAL CONDUCTIVITY

In the low-frequency limit, the frequency dependence of the measured temperature amplitude is governed solely by the thermal conductivity of the substrate (κ_s). Specifically, the substrate's peak temperature amplitude as a function of the angular heating frequency (ω_h) then becomes[66,89,90]

$$T_{s,\mathrm{in-phase}}(\omega_h) = \frac{P}{\pi l \kappa_s}(\mathrm{constant} - \ln \omega_h). \tag{B1}$$

Here, the constant term is independent of the heating frequency, and the substrate's thermal conductivity can be extracted from the slope of the temperature amplitude vs frequency plot. Notably, Eq. (B1) also applies to crystalline materials with cubic symmetry, where the thermal conductivity tensor reduces to diagonal form with κ_s as the sole independent parameter.[90] Estimates of the thermal conductivity of our silicon substrates for all measured samples are presented in Fig. 10, together with literature values for high-purity bulk single-crystalline silicon.[91] Our results show good

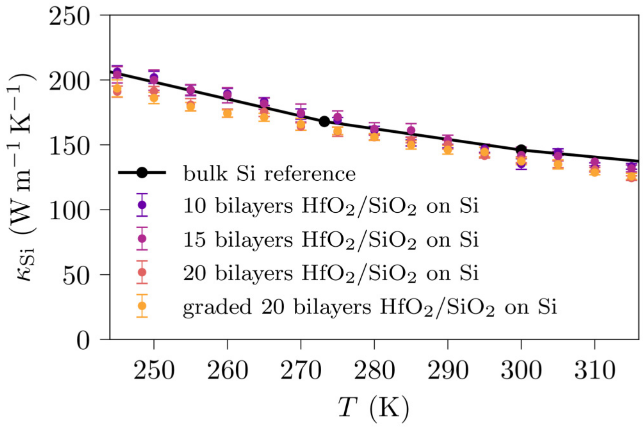

FIG. 10. Estimated thermal conductivity of the (p-type) single-crystalline silicon substrates [colored solid circles, electrical resistivity: $15 \pm 7\,\Omega$ cm corresponds to a low impurity concentration, ensuring high-purity single-crystalline silicon thermal behavior for validation[92,93]]. The data are compared to the reported literature value for high-purity bulk single-crystalline silicon digitally plotted from the tabulated reference data of Touloukian *et al.*[91] (black solid circle). The black line represents an interpolation of these tabulated values and serves as a guide for the eye.

agreement with established literature and demonstrate strong sample-to-sample reproducibility. Quantitatively, at 300 K, the average thermal conductivity of our Si substrates was determined to be $133 \pm 13\,\mathrm{W\,m^{-1}\,K^{-1}}$, which is in good agreement with the widely accepted bulk value[91] of $146 \pm 15\,\mathrm{W\,m^{-1}\,K^{-1}}$.

APPENDIX C: *3ω* MEASUREMENT SETUP VALIDATION: FREQUENCY SCALING OF THE *3ω* VOLTAGE SIGNAL AMPLITUDE

To further validate our measurement setup, we verified the fundamental cubic relationship between the measured peak 3ω voltage amplitude ($U_{3\omega}$) and the applied electrical peak 1ω current amplitude ($I_{1\omega}$). The relationship $U_{3\omega} \propto I_{1\omega}^3$ was consistently confirmed across a range of frequencies and temperatures, as shown in Fig. 11.

APPENDIX D: THEORETICAL FRAMEWORK FOR THERMAL TRANSPORT

The theoretical basis for thermal transport in electrically insulating materials posits that heat is carried by quantized atomic lattice vibrations. These quasiparticles follow Bose–Einstein statistics. The material's thermal conductivity is expressed as a sum over the contributions of individual vibrational modes (n),

$$\kappa(T) = \frac{1}{V}\sum_n C(\omega_n, T) D_n(T), \tag{D1}$$

where V is the sample volume, $C(\omega_n, T)$ is the specific heat of a single vibrational mode at angular frequency ω_n and temperature T, and $D_n(T)$ is the corresponding mode diffusivity.

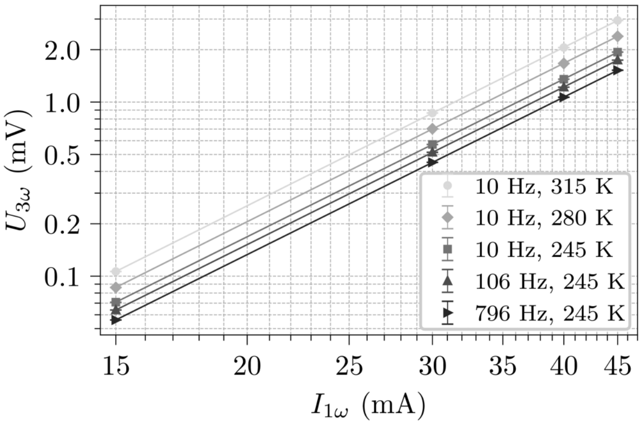

FIG. 11. $U_{3\omega}$ as a function of $I_{1\omega}$ for the graded 20-bilayer HfO_2/SiO_2 sample. The data, measured at various frequencies and temperatures (symbols), confirm the expected cubic relationship, $U_{3\omega} \propto I_{1\omega}^3$, as indicated by the linear fits (solid lines) with slopes of 3.01 ± 0.01 on this double-logarithmic scale.

1. Debye model

For our analysis, we model the vibrational properties of the amorphous constituent materials within the Debye framework. In this approximation, the vibrational density of states (DOS) for each acoustic branch[94] m (one longitudinal, two transverse) is given by

$$\mathrm{DOS}_m(\omega) = \frac{V\omega^2}{2\pi^2 v_m^3}\, 1_{[0,\omega_{D,m}]}(\omega), \tag{D2}$$

where V is the sample volume, v_m is the branch-specific speed of sound, and $\omega_{D,m}$ is the Debye cutoff frequency of acoustic branch m. Here, $1_{[a,b]}(\omega)$ denotes the indicator function that equals 1 if $\omega \in [a, b]$ and 0 otherwise.

The specific heat of a bosonic vibrational mode at angular frequency ω and temperature T follows the standard expression:[95]

$$C(\omega, T) = k_B \exp\left(\frac{\hbar\omega}{k_B T}\right)\left(\frac{\frac{\hbar\omega}{k_B T}}{\exp\left(\frac{\hbar\omega}{k_B T}\right) - 1}\right)^2, \tag{D3}$$

with k_B denoting Boltzmann's constant, $\hbar$ the reduced Planck constant, and T the temperature.

TABLE II. Material properties of amorphous HfO_2 and SiO_2 thin films. Atomic number densities were estimated from XRR mass densities assuming stoichiometry. Speeds of sound for amorphous SiO_2 are reproduced with permission from Cahill and Pohl, Phys. Rev. B: Condens. Matter **35**, 4067–4073 (1987). Copyright 1987 American Physical Society,[66] Love, Phys. Rev. Lett. **31**, 822–825 (1973). Copyright 1973 American Physical Society,[96] and Ivanda *et al.*, J. Raman Spectrosc. **38**, 647–659 (2007). Copyright 2007 John Wiley and Sons.[97] For amorphous HfO_2, the longitudinal speed was calculated using elastic modulus data reported by Fields *et al.*[98] The transverse speed of sound was assumed based on a value for crystalline HfO_2 nanoparticles[97] due to the absence of a published value for the amorphous thin film. The mean speed of sound is defined here as $v := \left(\frac{1}{3v_l^3} + \frac{2}{3v_t^3}\right)^{\frac{-1}{3}}$.

Thin film property	Amorphous HfO_2	Amorphous SiO_2
Mass density ($\mathrm{g\,cm^{-3}}$)	6.72 ± 0.04	2.28 ± 0.04
Atomic density ($\mathrm{nm^{-3}}$)	58 ± 3	69 ± 9
Longitudinal speed of sound v_l ($\mathrm{km s^{-1}}$)	4.97 ± 0.07[98]	5.8[66,96]
Transverse speed of sound v_t ($\mathrm{km s^{-1}}$)	2.4[97]	3.7[66,96]
Mean speed of sound v ($\mathrm{km s^{-1}}$)	2.7	4.1
Longitudinal Debye temperature $\Theta_{l,D}$ (K)	572	713
Transverse Debye temperature $\Theta_{t,D}$ (K)	277	448

The volumetric heat capacity is obtained by summing the contributions from all acoustic branches,

$$C_V(T) = 3nk_B \sum_m \left(\frac{T}{\Theta_{D,m}}\right)^3 \int_0^{\frac{\Theta_{D,m}}{T}} \frac{x^4 \exp(x)}{(\exp(x)-1)^2}\,\mathrm{d}x, \tag{D4}$$

where n is the atomic number density and $\Theta_{D,m}$ is the Debye temperature corresponding to the acoustic branch m. The material parameters used in our analysis are summarized in Table II.

2. Modeling the effective thermal conductivity

To interpret the effective through-plane thermal conductivity, $\kappa_{z,\mathrm{eff}}$, described by Eq. (5), we adopt a two-step modeling strategy. First, we estimate the intrinsic thermal conductivities of HfO_2 and SiO_2 using the minimum thermal conductivity model proposed by Cahill and Pohl.[56,66,67] In the second step, we account for interfacial effects by incorporating a finite thermal boundary conductance within the framework of the DMM.[68]

3. Minimum thermal conductivity model

Cahill and Pohl[56,66,67] extended the traditional understanding of thermal conductivity in amorphous solids by drawing on principles from both the Einstein[99,100] and Debye[101] models. Instead of a single Einstein oscillator frequency, they utilized the Debye DOS [Eq. (D2)]. Within this framework, they proposed a frequency-dependent mean free path for phonons in amorphous materials, given by

$$l_{\mathrm{MFP}} = \frac{\pi v}{\omega}, \tag{D5}$$

where v is the velocity of the vibrational mode of angular frequency ω. Consequently, they employed the following mode-specific diffusivity:

$$D(\omega) = \frac{1}{3} v l_{\mathrm{MFP}}(\omega). \tag{D6}$$

The total thermal conductivity, referred to in this context as the minimum thermal conductivity $\kappa_{\min}$, is subsequently obtained by integrating the contributions of all vibrational modes up to the Debye frequency and summing over all acoustic branches [the continuum limit of Eq. (D1)],

$$\kappa_{\min} = \sum_m \int_0^{\omega_{D,m}} \mathrm{DOS}_m(\omega) C(\omega, T) D_m(\omega) d\omega. \tag{D7}$$

Explicit evaluation of Eq. (D7) leads to the following expression:

$$\kappa_{\min} = \left(\frac{\pi}{6}\right)^{\left(\frac{1}{3}\right)} n^{\left(\frac{2}{3}\right)} k_B \sum_m v_m \left(\frac{T}{\Theta_{D,m}}\right)^2 \int_0^{\frac{\Theta_{D,m}}{T}} \frac{x^3 \exp(x)}{(\exp(x)-1)^2}\,\mathrm{d}x, \tag{D8}$$

where k_B is the Boltzmann constant, and the sum runs over the three acoustic branches m. $\Theta_{D,m}$ is the Debye temperature for each branch, estimated from an isotropic material with speed of sound v_m and atomic number density n. The necessary model parameters are summarized in Table II. Explicit evaluation of the minimum thermal conductivity model are presented as gray-dashed lines in Figs. 6 and 7.

4. Diffusive mismatch model (DMM)

Thus far, we have neglected the potential influence of the HfO_2/SiO_2 interface on the thermal transport. A common approach to model the influence of a material interface on the thermal transport is to introduce a finite interface thermal conductance, $G_{1,2}$, into the heat equation [see Eq. (1)].

Microscopically, $G_{1,2}$ is attributed to phonon scattering at the material interface. The DMM, introduced by Swartz and Pohl,[68] is a widely used framework in this context. The DMM assumes that every phonon incident on the interface is scattered diffusively and incoherently with uniform probability into any available phonon mode with the same frequency, independent of its site of origin or incoming wavevector. Consequently, the model calculates the thermal boundary conductance based solely on the phonon density of states and group velocities of the interfacing materials.

In our case, we want to follow the common approach to model the phonon density of states of our isotropic materials via the Debye model (see Appendix D 1). To ensure the highest attainable accuracy across the entire temperature range, we will not limit our calculations to the simplified low-temperature limit detailed in the original Swartz and Pohl publication.[68] Instead, we will utilize the full thermal integral within the DMM framework, retaining the respective Debye temperature cutoffs,

$$G_{1,2}(T) = \frac{1}{8\pi^2} k_B \left(\frac{k_B T}{\hbar}\right)^3 \int_0^{\infty} \frac{\prod_{i\in\{1,2\}} \sum_m \frac{1}{v_{i,m}^2} 1_{\left[0,\frac{\Theta_{D,i,m}}{T}\right]}(x)}{\sum_{i\in\{1,2\}} \sum_m \frac{1}{v_{i,m}^2} 1_{\left[0,\frac{\Theta_{D,i,m}}{T}\right]}(x)} \frac{x^4 \exp(x)}{(\exp(x)-1)^2}\,\mathrm{d}x. \tag{D9}$$

Here, k_B denotes the Boltzmann constant, T the temperature, $\hbar$ the reduced Planck constant, $\Theta_{D,i,m}$ the Debye temperature of material i and acoustic branch m, and $1_{[a,b]}(x)$ the indicator function. The necessary model parameters are summarized in Table II. Explicit simulations of the HfO_2/SiO_2 multilayer thermal conductivity, both with and without the DMM interface corrections, are presented in Figs. 6 and 7. It should be noted that generally the Debye DOS represents only a low-frequency approximation. Therefore, at elevated temperatures where higher frequency modes also become relevant, this model framework is expected to hold only qualitatively at best.

5. A short note on atomistic approaches

Atomistic approaches have substantially advanced the understanding of thermal transport in amorphous materials. In particular, the seminal harmonic Allen–Feldman model for glasses[57,102–104] or more recent formalisms such as the quasi-harmonic Green–Kubo[83,105–107] and Wigner transport equation methods,[108–110] which explicitly incorporate anharmonic effects, should be mentioned in this context. Unfortunately, the practical application of these advanced frameworks is severely constrained by computational scaling, which fundamentally limits their ability to capture long-wavelength transport phenomena in disordered materials. Modeling a domain equivalent to our nanolaminates (e.g., $200 \times 200 \times 200\,\text{nm}^3$, corresponding to at least $\sim 10^8$ atoms) remains computationally prohibitive. This system-size limitation is particularly restrictive at cryogenic temperatures, where the long-wavelength excitations dominate thermal transport.

REFERENCES

[1] C. Hu, J. Bokor, T.-J. King, E. Anderson, C. Kuo, K. Asano, H. Takeuchi, J. Kedzierski, W.-C. Lee, and D. Hisamoto, "FinFET—A self-aligned double-gate MOSFET scalable to 20 nm," IEEE Trans. Electron Devices **47**, 2320–2325 (2000).

[2] X. Huang, W.-C. Lee, C. Kuo, D. Hisamoto, L. Chang, J. Kedzierski, E. Anderson, H. Takeuchi, Y.-K. Choi, K. Asano, V. Subramanian, T.-J. King, J. Bokor, and C. Hu, "Sub-50 nm P-channel FinFET," IEEE Trans. Electron Devices **48**, 880–886 (2001).

[3] A. Samal, S. L. Tripathi, and S. K. Mohapatra, "A journey from bulk MOSFET to 3 nm and beyond," Trans. Electr. Electron. Mater. **21**, 443–455 (2020).

[4] M.-L. Chen, X. Sun, H. Liu, H. Wang, Q. Zhu, S. Wang, H. Du, B. Dong, J. Zhang, Y. Sun, S. Qiu, T. Alava, S. Liu, D.-M. Sun, and Z. Han, "A FinFET with one atomic layer channel," Nat. Commun. **11**, 1205 (2020).

[5] M. N. Reddy and D. K. Panda, "A comprehensive review on FinFET in terms of its device structure and performance matrices," Silicon **14**, 12015–12030 (2022).

[6] J. Kumar, S. Birla, and G. Agarwal, "A review on effect of various high-k dielectric materials on the performance of FinFET device," Mater. Today Proc. **79**, 297–302 (2023).

[7] L. Qin, C. Li, Y. Wei, G. Hu, J. Chen, Y. Li, C. Du, Z. Xu, X. Wang, and J. He, "Recent developments in negative capacitance gate-all-around field effect transistors: A review," IEEE Access **11**, 14028–14042 (2023).

[8] W. Liao, W. Qian, J. An, L. Liang, Z. Hu, J. Wang, and L. Yu, "High-performance gate-all-around field effect transistors based on orderly arrays of catalytic Si nanowire channels," Nano-Micro Lett. **17**, 154 (2025).

[9] M. Jin, C. Liu, J. Kim, J. Kim, S. Choo, Y. Kim, H. Shim, L. Zhang, K.-J. Nam, J. Park, S. Pae, and H. Lee, "Hot carrier reliability characterization in consideration of self-heating in finfet technology," in *2016 IEEE International Reliability Physics Symposium (IRPS)* (IEEE, 2016), pp. 2A–2–1–2A–2–5.

[10] A. Kerber, "Reliability of metal gate/high-k devices and its impact on CMOS technology scaling," MRS Adv. **2**, 2973–2982 (2017).

[11] X. Liu, W. Chen, L. Cai, G. Du, and X. Zhang, "Self-heating induced variability and reliability in advanced logic devices and circuits," in *2019 IEEE 13th International Conference on ASIC (ASICON)* (IEEE, 2019), pp. 1–4.

[12] V. A. Chhabria and S. S. Sapatnekar, "Impact of self-heating on performance and reliability in FinFET and GAAFET designs," in *20th International Symposium on Quality Electronic Design (ISQED)* (IEEE, 2019), pp. 235–240.

[13] J. Wu, H. Qi, and Q. Zhao, "Self-heating effect of gate-all-around FETs: A review," Appl. Comput. Eng. **168**, 127–138 (2025).

[14] F. Zahoor, T. Z. Azni Zulkifli, and F. A. Khanday, "Resistive random access memory (RRAM): An overview of materials, switching mechanism, performance, multilevel cell (MLC) storage, modeling, and applications," Nanoscale Res. Lett. **15**, 90 (2020).

[15] J. H. Yoon, Y.-W. Song, W. Ham, J.-M. Park, and J.-Y. Kwon, "A review on device requirements of resistive random access memory (RRAM)-based neuromorphic computing," APL Mater. **11**, 090701 (2023).

[16] F. Zahoor, A. Nisar, U. I. Bature, H. Abbas, F. Bashir, A. Chattopadhyay, B. K. Kaushik, A. Alzahrani, and F. A. Hussin, "An overview of critical applications of resistive random access memory," Nanoscale Adv. **6**, 4980–5006 (2024).

[17] S. Deshmukh, M. M. Rojo, E. Yalon, S. Vaziri, C. Koroglu, R. Islam, R. A. Iglesias, K. Saraswat, and E. Pop, "Direct measurement of nanoscale filamentary hot spots in resistive memory devices," Sci. Adv. **8**, eabk1514 (2022).

[18] A. Sarantopoulos, K. Lange, F. Rivadulla, S. Menzel, and R. Dittmann, "Resistive switching acceleration induced by thermal confinement," Adv. Electron. Mater. **11**, 2400555 (2025).

[19] A. Gooran-Shoorakchaly, S. S. Sharif, and Y. M. Banad, "Investigating the effect of electrical and thermal transport properties on oxide-based memristors performance and reliability," Sci. Rep. **15**, 18646 (2025).

[20] L. M. K. Vandersypen, H. Bluhm, J. S. Clarke, A. S. Dzurak, R. Ishihara, A. Morello, D. J. Reilly, L. R. Schreiber, and M. Veldhorst, "Interfacing spin qubits in quantum dots and donors—Hot, dense, and coherent," npj Quantum Inf. **3**, 34 (2017).

[21] D. J. Reilly, "Challenges in scaling-up the control interface of a quantum computer," in *2019 IEEE International Electron Devices Meeting (IEDM)* (IEEE, 2019), pp. 31.7.1–31.7.6.

[22] S. Krinner, S. Storz, P. Kurpiers, P. Magnard, J. Heinsoo, R. Keller, J. Lütolf, C. Eichler, and A. Wallraff, "Engineering cryogenic setups for 100-qubit scale superconducting circuit systems," EPJ Quantum Technol. **6**, 2 (2019).

[23] S. J. Pauka, K. Das, R. Kalra, A. Moini, Y. Yang, M. Trainer, A. Bousquet, C. Cantaloube, N. Dick, G. C. Gardner, M. J. Manfra, and D. J. Reilly, "A cryogenic CMOS chip for generating control signals for multiple qubits," Nat. Electron. **4**, 64–70 (2021).

[24] H. Bluhm, "Isolator für kryoelektrische chips bei extrem niedrigen temperaturen unter 10 K," International Patent WO 2023/031477 A1 (9 March 2023), available at https://patents.google.com/patent/WO2023031477A1/de.

[25] C. Zota, A. Ferraris, E. Cha, M. Prathapan, P. Mueller, and E. Leobandung, "Energy-efficient computing at cryogenic temperatures," Nat. Electron. **7**, 966–974 (2024).

[26] M. Künne, A. Willmes, M. Oberländer, C. Gorjaew, J. D. Teske, H. Bhardwaj, M. Beer, E. Kammerloher, R. Otten, I. Seidler, R. Xue, L. R. Schreiber, and H. Bluhm, "The spinbus architecture for scaling spin qubits with electron shuttling," Nat. Commun. **15**, 4977 (2024).

[27] Z. Bao, Y. Li, Z. Wang, J. Wang, J. Yang, H. Xiong, Y. Song, Y. Wu, H. Zhang, and L. Duan, "A cryogenic on-chip microwave pulse generator for large-scale superconducting quantum computing," Nat. Commun. **15**, 5958 (2024).

[28] J. Franco, J.-F. de Marneffe, A. Vandooren, Y. Kimura, L. Nyns, Z. Wu, A.-M. El-Sayed, M. Jech, D. Waldhoer, D. Claes, H. Arimura, L.-Å. Ragnarsson, V. Afanas'ev, A. Stesmans, N. Horiguchi, D. Linten, T. Grasser, and B. Kaczer, "Atomic hydrogen exposure to enable high-quality low-temperature SiO_2 with excellent pMOS NBTI reliability compatible with 3D sequential tier stacking," in *2020 IEEE International Electron Devices Meeting (IEDM)* (IEEE, 2020), pp. 31.2.1–31.2.4.

[29] J. Franco, H. Arimura, J.-F. de Marneffe, Z. Wu, A. Vandooren, L.-Å. Ragnarsson, E. D. Litta, N. Horiguchi, K. Croes, D. Linten, V. Afanas'ev, T. Grasser, and B. Kaczer, "Low-temperature atomic and molecular hydrogen anneals for enhanced chemical SiO_2 IL quality in low thermal budget RMG stacks," in *2021 IEEE International Electron Devices Meeting (IEDM)* (IEEE, 2021), pp. 31.4.1–31.4.4.

[30] J. Franco, H. Arimura, S. Brus, E. Dentoni Litta, K. Croes, N. Horiguchi, and B. Kaczer, "Impact of work function metal stacks on the performance and reliability of multi-V_{th} RMG CMOS technology," Solid State Electron. **216**, 108929 (2024).

[31] L. Verschueren, G. Eneman, S. Yang, J. Bömmels, P. Matagne, K. B. Cahueñas, A. Sharma, D. Abdi, H. Mertens, G. Mirabelli, and G. Hellings, "Extending the gate-all-around (GAA) era to the A10 node: Outer wall forksheet enabling full channel strain and superior gate control," in *2025 Symposium on VLSI Technology and Circuits (VLSI Technology and Circuits)* (IEEE, 2025), pp. 1–3.

[32] D. G. Schlom, S. Guha, and S. Datta, "Gate oxides beyond SiO_2," MRS Bull. **33**, 1017–1025 (2008).

[33] J. H. Choi, Y. Mao, and J. P. Chang, "Development of hafnium based high-k materials—A review," Mater. Sci. Eng. R Rep. **72**, 97–136 (2011).

[34] R. Rammula, J. Aarik, H. Mändar, P. Ritslaid, and V. Sammelselg, "Atomic layer deposition of HfO_2: Effect of structure development on growth rate, morphology and optical properties of thin films," Appl. Surf. Sci. **257**, 1043–1052 (2010).

[35] X. Nie, F. Ma, D. Ma, and K. Xu, "Thermodynamics and kinetic behaviors of thickness-dependent crystallization in high-k thin films deposited by atomic layer deposition," J. Vac. Sci. Technol. A **33**, 01A140 (2015).

[36] K. Kukli, J. Aarik, M. Ritala, T. Uustare, T. Sajavaara, J. Lu, J. Sundqvist, A. Aidla, L. Pung, A. Hårsta, and M. Leskelä, "Effect of selected atomic layer deposition parameters on the structure and dielectric properties of hafnium oxide films," J. Appl. Phys. **96**, 5298–5307 (2004).

[37] N. T. Gabriel and J. J. Talghader, "Thermal conductivity and refractive index of hafnia-alumina nanolaminates," J. Appl. Phys. **110**, 043526 (2011).

[38] S. Ali, T. Juntunen, S. Sintonen, O. M. E. Ylivaara, R. L. Puurunen, H. Lipsanen, I. Tittonen, and S.-P. Hannula, "Thermal conductivity of amorphous Al_2O_3/TiO_2 nanolaminates deposited by atomic layer deposition," Nanotechnology **27**, 445704 (2016).

[39] S. W. Fong, A. Sood, L. Chen, N. Kumari, M. Asheghi, K. E. Goodson, G. A. Gibson, and H.-S. P. Wong, "Thermal conductivity measurement of amorphous dielectric multilayers for phase-change memory power reduction," J. Appl. Phys. **120**, 015103 (2016).

[40] R. M. Costescu, D. G. Cahill, F. H. Fabreguette, Z. A. Sechrist, and S. M. George, "Ultra-low thermal conductivity in W/Al_2O_3 nanolaminates," Science **303**, 989–990 (2004).

[41] V. Rawat, Y. K. Koh, D. G. Cahill, and T. D. Sands, "Thermal conductivity of (Zr,W)N/ScN metal/semiconductor multilayers and superlattices," J. Appl. Phys. **105**, 024909 (2009).

[42] Z. Li, S. Tan, E. Bozorg-Grayeli, T. Kodama, M. Asheghi, G. Delgado, M. Panzer, A. Pokrovsky, D. Wack, and K. E. Goodson, "Phonon dominated heat conduction normal to Mo/Si multilayers with period below 10 nm," Nano Lett. **12**, 3121–3126 (2012).

[43] E. Dechaumphai, D. Lu, J. J. Kan, J. Moon, E. E. Fullerton, Z. Liu, and R. Chen, "Ultralow thermal conductivity of multilayers with highly dissimilar debye temperatures," Nano Lett. **14**, 2448–2455 (2014).

[44] B. Saha, Y. R. Koh, J. Comparan, S. Sadasivam, J. L. Schroeder, M. Garbrecht, A. Mohammed, J. Birch, T. Fisher, A. Shakouri, and T. D. Sands, "Cross-plane thermal conductivity of (Ti,W)N/(Al,Sc)N metal/semiconductor superlattices," Phys. Rev. B **93**, 045311 (2016).

[45] A. Kovalev, D. Wainstein, V. Vakhrushev, R. Gago, and J. L. Endrino, "Anomalous heat transport in nanolaminate metal/oxide multilayer coatings: Plasmon and phonon excitations," Coatings **10**, 260 (2020).

[46] W. Zheng, B. Huang, and Y. K. Koh, "Ultralow thermal conductivity and thermal diffusivity of graphene/metal heterostructures through scarcity of low-energy modes in graphene," ACS Appl. Mater. Interfaces **12**, 9572–9579 (2020).

[47] S.-M. Lee, D. G. Cahill, and R. Venkatasubramanian, "Thermal conductivity of Si–Ge superlattices," Appl. Phys. Lett. **70**, 2957–2959 (1997).

[48] W. S. Capinski, H. J. Maris, T. Ruf, M. Cardona, K. Ploog, and D. S. Katzer, "Thermal-conductivity measurements of GaAs/AlAs superlattices using a picosecond optical pump-and-probe technique," Phys. Rev. B **59**, 8105–8113 (1999).

[49] T. Borca-Tasciuc, W. Liu, J. Liu, T. Zeng, D. W. Song, C. D. Moore, G. Chen, K. L. Wang, M. S. Goorsky, T. Radetic, R. Gronsky, T. Koga, and M. S. Dresselhaus, "Thermal conductivity of symmetrically strained Si/Ge superlattices," Superlattices Microstruct. **28**, 199–206 (2000).

[50] Y. K. Koh, Y. Cao, D. G. Cahill, and D. Jena, "Heat–transport mechanisms in superlattices," Adv. Funct. Mater. **19**, 610–615 (2009).

[51] M. N. Luckyanova, J. Garg, K. Esfarjani, A. Jandl, M. T. Bulsara, A. J. Schmidt, A. J. Minnich, S. Chen, M. S. Dresselhaus, Z. Ren, E. A. Fitzgerald, and G. Chen, "Coherent phonon heat conduction in superlattices," Science **338**, 936–939 (2012).

[52] J. Ravichandran, A. K. Yadav, R. Cheaito, P. B. Rossen, A. Soukiassian, S. J. Suresha, J. C. Duda, B. M. Foley, C.-H. Lee, Y. Zhu, A. W. Lichtenberger, J. E. Moore, D. A. Muller, D. G. Schlom, P. E. Hopkins, A. Majumdar, R. Ramesh, and M. A. Zurbuchen, "Crossover from incoherent to coherent phonon scattering in epitaxial oxide superlattices," Nat. Mater. **13**, 168–172 (2014).

[53] R. Cheaito, C. A. Polanco, S. Addamane, J. Zhang, A. W. Ghosh, G. Balakrishnan, and P. E. Hopkins, "Interplay between total thickness and period thickness in the phonon thermal conductivity of superlattices from the nanoscale to the microscale: Coherent versus incoherent phonon transport," Phys. Rev. B **97**, 085306 (2018).

[54] J. M. Ziman, *Electrons and Phonons: The Theory of Transport Phenomena in Solids*, Oxford Classic Texts in the Physical Sciences (Clarendon, Oxford, 1960).

[55] J. J. Freeman and A. C. Anderson, "Thermal conductivity of amorphous solids," Phys. Rev. B: Condens. Matter **34**, 5684–5690 (1986).

[56] D. G. Cahill and R. O. Pohl, "Lattice vibrations and heat transport in crystals and glasses," Annu. Rev. Phys. Chem. **39**, 93–121 (1988).

[57] P. B. Allen, J. L. Feldman, J. Fabian, and F. Wooten, "Diffusons, locons and propagons: Character of atomic vibrations in amorphous Si," Philos. Mag. B **79**, 1715–1731 (1999).

[58] N. Tambo, Y. Liao, C. Zhou, E. M. Ashley, K. Takahashi, P. F. Nealey, Y. Naito, and J. Shiomi, "Ultimate suppression of thermal transport in amorphous silicon nitride by phononic nanostructure," Sci. Adv. **6**, eabc0075 (2020).

[59] W. Peng and R. B. Wilson, "Nanoscale laser flash measurements of diffuson transport in amorphous Ge and Si," APL Mater. **10**, 041111 (2022).

[60] Z. Zeng, X. Liang, Z. Fan, Y. Chen, M. Simoncelli, and B. Cheng, "Thermal transport of amorphous hafnia across the glass transition," ACS Mater. Lett. **7**, 2695–2701 (2025).

[61] J. Moon and Z. Tian, "Crystal-like thermal transport in amorphous carbon," npj Comput. Mater. **11**, 137 (2025).

[62] S.-M. Lee and D. G. Cahill, "Heat transport in thin dielectric films," J. Appl. Phys. **81**, 2590–2595 (1997).

[63] J. H. Kim, A. Feldman, and D. Novotny, "Application of the three omega thermal conductivity measurement method to a film on a substrate of finite thickness," J. Appl. Phys. **86**, 3959–3963 (1999).

[64] M. A. Panzer, M. Shandalov, J. A. Rowlette, Y. Oshima, Y. W. Chen, P. C. McIntyre, and K. E. Goodson, "Thermal properties of ultrathin hafnium oxide gate dielectric films," IEEE Electron Device Lett. **30**, 1269–1271 (2009).

[65] E. A. Scott, J. T. Gaskins, S. W. King, and P. E. Hopkins, "Thermal conductivity and thermal boundary resistance of atomic layer deposited high-k dielectric aluminum oxide, hafnium oxide, and titanium oxide thin films on silicon," APL Mater. **6**, 058302 (2018).

[66] D. G. Cahill and R. O. Pohl, "Thermal conductivity of amorphous solids above the plateau," Phys. Rev. B: Condens. Matter **35**, 4067–4073 (1987).

[67] D. G. Cahill and R. O. Pohl, "Heat flow and lattice vibrations in glasses," Solid State Commun. **70**, 927–930 (1989).

[68] E. T. Swartz and R. O. Pohl, "Thermal boundary resistance," Rev. Mod. Phys. **61**, 605–668 (1989).

[69] A. Glavic and M. Björck, "GenX3: The latest generation of an established tool," J. Appl. Crystallogr. **55**, 1063–1071 (2022).

[70] C. D. Wagner, L. E. Davis, M. V. Zeller, J. A. Taylor, R. H. Raymond, and L. H. Gale, "Empirical atomic sensitivity factors for quantitative analysis by electron spectroscopy for chemical analysis," Surf. Interface Anal. **3**, 211–225 (1981).

[71] A. Jain, S. P. Ong, G. Hautier, W. Chen, W. D. Richards, S. Dacek, S. Cholia, D. Gunter, D. Skinner, G. Ceder, and K. A. Persson, "Commentary: The materials project: A materials genome approach to accelerating materials innovation," APL Mater. **1**, 011002 (2013).

[72] G. Jozwiak, A. Henrykowski, A. Masalska, T. Gotszalk, I. Ritz, and H. Steigmann, "The regularized blind tip reconstruction algorithm as a scanning probe microscopy tip metrology method," CoRR abs/1105.1472 (2011).

[73] D. G. Cahill, M. Katiyar, and J. R. Abelson, "Thermal conductivity of *a*-Si:H thin films," Phys. Rev. B: Condens. Matter **50**, 6077–6081 (1994).

[74] C. Dames, *Measuring the Thermal Conductivity of Thin Films: 3 Omega and Related Electrothermal Methods*, Begell Digital Library Vol. 16 (Begell House, Inc., Redding, CT, 2013).

[75] C. Xing, C. Jensen, T. Munro, B. White, H. Ban, and M. Chirtoc, "Accurate thermal property measurement of fine fibers by the 3-omega technique," Appl. Therm. Eng. **73**, 317–324 (2014).

[76] Y. Wang, H. Huang, and X. Ruan, "Decomposition of coherent and incoherent phonon conduction in superlattices and random multilayers," Phys. Rev. B **90**, 165406 (2014).

[77] B. Qiu, G. Chen, and Z. Tian, "Effects of aperiodicity and roughness on coherent heat conduction in superlattices," Nanoscale Microscale Thermophys. Eng. **19**, 272–278 (2015).

[78] T. Juntunen, O. Vänskä, and I. Tittonen, "Anderson localization quenches thermal transport in aperiodic superlattices," Phys. Rev. Lett. **122**, 105901 (2019).

[79] T. Ma, C.-T. Lin, and Y. Wang, "The dimensionality effect on phonon localization in graphene/hexagonal boron nitride superlattices," 2D Mater. **7**, 035029 (2020).

[80] P. Chakraborty, Y. Liu, T. Ma, X. Guo, L. Cao, R. Hu, and Y. Wang, "Quenching thermal transport in aperiodic superlattices: A molecular dynamics and machine learning study," ACS Appl. Mater. Interfaces **12**, 8795–8804 (2020).

[81] M. N. Luckyanova, J. Mendoza, H. Lu, B. Song, S. Huang, J. Zhou, M. Li, Y. Dong, H. Zhou, J. Garlow, L. Wu, B. J. Kirby, A. J. Grutter, A. A. Puretzky, Y. Zhu, M. S. Dresselhaus, A. Gossard, and G. Chen, "Phonon localization in heat conduction," Sci. Adv. **4**, eaat9460 (2018).

[82] Y. S. Touloukian, R. W. Powell, C. Y. Ho, and P. G. Klemens, *Thermophysical Properties of Matter: The TPRC Data Series*, 3rd ed., Thermophysical Properties of Matter Vol. 2 (IFI, New York, 1978).

[83] A. Fiorentino, P. Pegolo, and S. Baroni, "Hydrodynamic finite-size scaling of the thermal conductivity in glasses," npj Comput. Mater. **9**, 157 (2023).

[84] X. Zhu, J. Sun, Y. Xiong, S. Li, and X. Liu, "Research on thermal transport mechanism of amorphous hafnia based on quasi-harmonic Green-Kubo theory combined with hydrodynamic extrapolation method," Acta Phys. Sin. **74**, 116302 (2025).

[85] T. Ma, P. Chakraborty, X. Guo, L. Cao, and Y. Wang, "First-principles modeling of thermal transport in materials: Achievements, opportunities, and challenges," Int. J. Thermophys. **41**, 9 (2020).

[86] R. Hu, S. Iwamoto, L. Feng, S. Ju, S. Hu, M. Ohnishi, N. Nagai, K. Hirakawa, and J. Shiomi, "Machine-learning-optimized aperiodic superlattice minimizes coherent phonon heat conduction," Phys. Rev. X **10**, 021050 (2020).

[87] S. Erfantalab, G. Parish, and A. Keating, "Determination of thermal conductivity, thermal diffusivity and specific heat capacity of porous silicon thin films using the 3 omega method," Int. J. Heat Mass Transfer **184**, 122346 (2022).

[88] F. P. Incropera, *Fundamentals of Heat and Mass Transfer*, 6th ed. (Wiley, Hoboken, NJ, 2007).

[89] D. G. Cahill, "Thermal conductivity measurement from 30 to 750 K: The 3ω method," Rev. Sci. Instrum. **61**, 802–808 (1990).

[90] V. Mishra, C. L. Hardin, J. E. Garay, and C. Dames, "A 3 omega method to measure an arbitrary anisotropic thermal conductivity tensor," Rev. Sci. Instrum. **86**, 054902 (2015).

[91] Y. S. Touloukian, R. W. Powell, C. Y. Ho, and P. G. Klemens, *Thermal Conductivity: Metallic Elements and Alloys*, Thermophysical Prosperties of Matter Vol. 1 (Springer US, Boston, MA, 1970).

[92] X. Fan, Z. Zhang, J. Zhu, K. Yuan, J. Zhou, X. Zhang, and D. Tang, "Systematic investigations on doping dependent thermal transport properties of single crystal silicon by time-domain thermoreflectance measurements," Int. J. Therm. Sci. **177**, 107558 (2022).

[93] B. Liao, B. Qiu, J. Zhou, S. Huberman, K. Esfarjani, and G. Chen, "Significant reduction of lattice thermal conductivity by the electron-phonon interaction in silicon with high carrier concentrations: A first-principles study," Phys. Rev. Lett. **114**, 115901 (2015).

[94] L. D. Landau and E. M. Lifschitz, *Theory of Elasticity*, 3rd ed. (Elsevier Science, Oxford, 1984), Vol. 7.

[95] C. Kittel, *Introduction to Solid State Physics*, 8th ed. (Wiley, Hoboken, NJ, 2005).

[96] W. F. Love, "Low-temperature thermal brillouin scattering in fused silica and borosilicate glass," Phys. Rev. Lett. **31**, 822–825 (1973).

[97] M. Ivanda, K. Furić, S. Musić, M. Ristić, M. Gotić, D. Ristić, A. M. Tonejc, I. Djerdj, M. Mattarelli, M. Montagna, F. Rossi, M. Ferrari, A. Chiasera, Y. Jestin, G. C. Righini, W. Kiefer, and R. R. Gonçalves, "Low wavenumber Raman scattering of nanoparticles and nanocomposite materials," J. Raman Spectrosc. **38**, 647–659 (2007).

[98] S. S. Fields, D. H. Olson, S. T. Jaszewski, C. M. Fancher, S. W. Smith, D. A. Dickie, G. Esteves, M. D. Henry, P. S. Davids, P. E. Hopkins, and J. F. Ihlefeld, "Compositional and phase dependence of elastic modulus of crystalline and amorphous $Hf_{1-x}Zr_xO_2$ thin films," Appl. Phys. Lett. **118**, 102901 (2021).

[99] A. Einstein, "Die plancksche theorie der strahlung und die theorie der spezifischen wärme," Ann. Phys. **327**, 180–190 (1907).

[100] A. Einstein, "Elementare Betrachtungen über die thermische Molekularbewegung in festen Körpern," Ann. Phys. **340**, 679–694 (1911).

[101] P. Debye, "Zur theorie der spezifischen wärmen," Ann. Phys. **344**, 789–839 (1912).

[102] P. B. Allen and J. L. Feldman, "Thermal conductivity of glasses: Theory and application to amorphous Si," Phys. Rev. Lett. **62**, 645–648 (1989).

[103] P. B. Allen and J. L. Feldman, "Thermal conductivity of disordered harmonic solids," Phys. Rev. B: Condens. Matter **48**, 12581–12588 (1993).

[104] J. L. Feldman, M. D. Kluge, P. B. Allen, and F. Wooten, "Thermal conductivity and localization in glasses: Numerical study of a model of amorphous silicon," Phys. Rev. B: Condens. Matter **48**, 12589–12602 (1993).

[105] L. Isaeva, G. Barbalinardo, D. Donadio, and S. Baroni, "Modeling heat transport in crystals and glasses from a unified lattice-dynamical approach," Nat. Commun. **10**, 3853 (2019).

[106] A. Fiorentino and S. Baroni, "From Green-Kubo to the full boltzmann kinetic approach to heat transport in crystals and glasses," Phys. Rev. B **107**, 054311 (2023).

[107] A. Fiorentino, E. Drigo, S. Baroni, and P. Pegolo, "Unearthing the foundational role of anharmonicity in heat transport in glasses," Phys. Rev. B **109**, 224202 (2024).

[108] M. Simoncelli, N. Marzari, and F. Mauri, "Unified theory of thermal transport in crystals and glasses," Nat. Phys. **15**, 809–813 (2019).

[109] M. Simoncelli, N. Marzari, and F. Mauri, "Wigner formulation of thermal transport in solids," Phys. Rev. X **12**, 041011 (2022).

[110] M. Simoncelli, F. Mauri, and N. Marzari, "Thermal conductivity of glasses: First-principles theory and applications," npj Comput. Mater. **9**, 106 (2023).